LUND UNIVERSITY

Characterization of a double-sided silicon strip detector autoradiography system.

Örbom, Anders; Ahlstedt, Jonas; Serén, Tom; Auterinen, Iiro; Kotiluoto, Petri; Hauge, Håvard; Östlund, Karl; Olafsen, Tove; Wu, Anna M; Dahlbom, Magnus; Strand, Sven-Erik

Link to publication

Characterization of a Double-sided Silicon Strip Detector Autoradiography System

Anders Örbom[1], Jonas Ahlstedt[1], Tom Serén[2], Iiro Auterinen[2], Petri Kotiluoto[2], Håvard Hauge[3], Karl Östlund[1], Tove Olafsen[4], Anna M. Wu[4], Magnus Dahlbom[4], Sven-Erik Strand[1]

[1]Department of Medical Radiation Physics, Lund University, Lund, Sweden

[2]VTT Technical Research Centre of Finland, Finland

[3]Biomolex AS, Oslo, Norway

[4]Department of Molecular and Medical Pharmacology, David Geffen School of Medicine at UCLA, Los Angeles, CA, USA

Corresponding Author: Anders Örbom, Medical Radiation Physics, Lund University, Barngatan 2:1, SE-22185 Lund, Sweden, Tel: +46 46 222 0839, Fax: +46 46 178 540, E-mail: anders.orbom@med.lu.se [new email as of 2015: anders.oerbom@uni-wuerzburg.de]

ABSTRACT

Purpose

The most commonly used technology currently used for autoradiography is storage phosphor screens, which has many benefits such as a large field of view but lacks particle-counting detection of the time and energy of each detected radionuclide decay. A number of alternative designs, using either solid state or scintillator detectors, have been developed to address these issues. The aim of this study is to characterize the imaging performance of one such instrument, a double-sided silicon strip detector (DSSD) system for digital autoradiography. A novel aspect of this work is that the instrument, in contrast to previous prototype systems using the same detector type, provides the ability for user accessible imaging with higher throughput. Studies were performed to compare its spatial resolution to that of storage

phosphor screens and test the implementation of multi-radionuclide *ex vivo* imaging in a mouse preclinical animal study.

Methods

Detector background counts were determined by measuring a non-radioactive sample slide for 52 h. Energy spectra and detection efficiency were measured for 7 commonly used radionuclides under representative conditions for tissue imaging. System dead time was measured by imaging ^{18}F samples of at least 5 kBq and studying the changes in count rate over time. A line source of ^{58}Co was manufactured by irradiating a 10 μm nickel wire with fast neutrons in a research reactor. Samples of this wire were imaged in both the DSSD and storage phosphor screen systems and the full width at half maximum (FWHM) measured for the line profiles. Multi-radionuclide imaging was employed in a two animal study to examine the intra-tumoral distribution of a ^{125}I-labeled monoclonal antibody and a ^{131}I-labeled engineered fragment (diabody) injected in the same mouse, both targeting carcinoembryonic antigen.

Results

Detector background was 1.81 x 10^{-6} counts per second per 50 μm x 50 μm pixel. Energy spectra and detection efficiency were successfully measured for 7 radionuclides. The system dead time was measured to be 59 μs and FWHM for a ^{58}Co line source was 154 ±14 μm for the DSSD system and 343 ±15 μm for the storage phosphor system. Separation of the contributions from ^{125}I and ^{131}I were performed on autoradiography images of tumor sections.

Conclusion

This study has shown that a DSSD system can be beneficially applied for digital autoradiography with simultaneous multi-radionuclide imaging capability. The system has a

low background signal, ability to image both low and high activity samples, and a good energy resolution.

1. INTRODUCTION

Autoradiography is in widespread use in drug development and preclinical research[1]. Whereas the classic method of using autoradiographic film offers very good spatial resolution, it suffers from low sensitivity, limited dynamic range and poor linearity, which led to the search for alternative technologies[2]. The most commonly used technology today is storage phosphor screens. During exposure to ionizing radiation, $BaFBr:Eu^{2+}$ crystals are ionized to $BaFBr:Eu^{3+}$. The process is reversed during read-out where irradiation with a red laser releases the stored energy at each coordinate as visible light, which can then be quantified[3, 4]. However neither film or storage phosphor methods provide real-time measurement data that would enable a quick evaluation of the activity in a sample, required imaging time, sample thickness etc. This is especially important when using short-lived radionuclides such as ^{18}F or ^{11}C. Neither do these integrating systems contain any information on the deposited energy or time point for each registered interaction which would enable simultaneous imaging and subsequent separation of the signals from several different radionuclides. To address this, a number of alternative, for the most part particle-counting, detector technologies have been developed. These include systems where a charge-coupled device (CCD) is used to register light generated by a sample in contact with either a scintillator sheet[5], an ultra-thin phosphor layer[6], a silver-activated zinc sulfide phosphor sheet[7], or by exposure to a parallel plate avalanche chamber[5]. Systems based on microchannel plates have also been developed[8, 9] as well as a number of solid-state, silicon detectors based on back-thinned CCD and CMOS sensors[10, 11], silicon pixel detectors[12] or silicon strip detectors[13, 14].

One such system, the Biomolex 700 imager (Biomolex, Oslo, Norway), which is a double-sided silicon strip detector (DSSD) system originally designed for microarray imaging has been evaluated for its potential to be used for digital autoradiography. The system hardware and software has recently been further developed and there is no prior characterization of the instrument in its current form in the literature. The system is also generally available, in contrast to most of the systems referenced and has recently been employed in several biological studies[15-17]. The novel aspects of this work consist of characterization and demonstration of an instrument that in contrast to prior silicon strip based autoradiography systems[13] has the potential for comparably high throughput routine imaging of preclinical or clinical tissue samples. This due to the FOV of the detector that while small, covers a normal sample slide in contrast to previous systems[13, 14], the automatic sample changer system which allows for scheduling of serial imaging without constant user supervision, and accessible user interface. We also demonstrate the usefulness of the instrument in the context of employing autoradiography as a complement to *in vivo* preclinical molecular imaging using radiolabeled tracers, determining the characteristics for a wide range of radionuclides relevant to this setting. The aim of this study therefore is to characterize the imaging performance of the system for digital autoradiography and to directly compare the spatial resolution of the DSSD system with storage phosphor screens.

2. METHODS AND MATERIALS

2.A. System Design

The detector module, outlined in Figure 1A, consists of a double-sided silicon strip detector (Hamamatsu Photonics, Hamamatsu City, Japan) with an area of 32 mm x 64 mm containing 560 vertical and 1260 horizontal strips on each side of the 300 μm thick silicon core of the detector with a centre to centre distance of 50 μm between adjacent strips, resulting in a grid

pattern allowing an intrinsic resolution of 50 μm x 50 μm pixels The silicon core contains the epi-layer where a homogenous electrical field is sustained by the conducting strips on each side of the detector.

Since the strips on one side are defined as positive (p-side) and the strips on the other side are defined as negative (n-side), a current induced by a particle interaction will generate a positive and a negative charge on opposite sides on the detector. The detector is cooled to 20°C during operation using a Peltier element. The ASIC, VATAGP chip, is a 128 channel self-trigging chip with CMOS VLSI technology dedicated to the read-out of microstrip detectors. Directly incoming β-particles of energies up to approximately 230 keV are fully absorbed by the detector and at higher energies a dE/dx spectrum is measured. Particles hitting the detector at an angle deposit somewhat more energy before leaving the epi-layer. A protective layer, 1 um of silicone oxide (SiO_2), on top of the detector prevents detection of very low-energy electrons such as those emitted by ^3H which are fully absorbed before reaching the detector. Additionally, a 15-20 keV threshold for detected events is set to suppress detector noise. The maximum frame rate at which the detector can be read out is 10^4 events per second. A registered charge on one side of the detector is only registered as an event if a charge is registered in the opposite plane within a time frame of a few nanoseconds. If no coincidence is registered or more than one coincidence is registered the signal will be classified as noise and discarded. When the charge is distributed over several strips, the strips with the highest read-out charge on either side of the detector determine the x and y position. For each detected event the energy and the position is registered and displayed in real-time in the read-out software. The measured energy is defined as the sum of energies in the x and y position strips plus its closest neighboring strips. Inclusion of two neighboring strips is chosen as standard by manufacturer, but can be modified by the user. Use of more neighbors may more accurately measure the total deposited energy but will reduce the read-out frame rate, since

the readout time will be prolonged. The total number of events detected is registered each minute during measurement, allowing detected events to be time-stamped with a 1 minute precision. Imaging data can be exported in either binary format or in list-mode as a text file. Biological samples to be imaged, usually of around 10 μm thickness, are placed on standard microscope glass slides (75 mm x 25 mm) that are covered with a 3 μm Mylar foil before being applied to the detector. The sample area of these slides is encompassed by the detector field of view. The samples can be loaded separately or by the use of a 12-slot sample changer as seen in Figure 1.
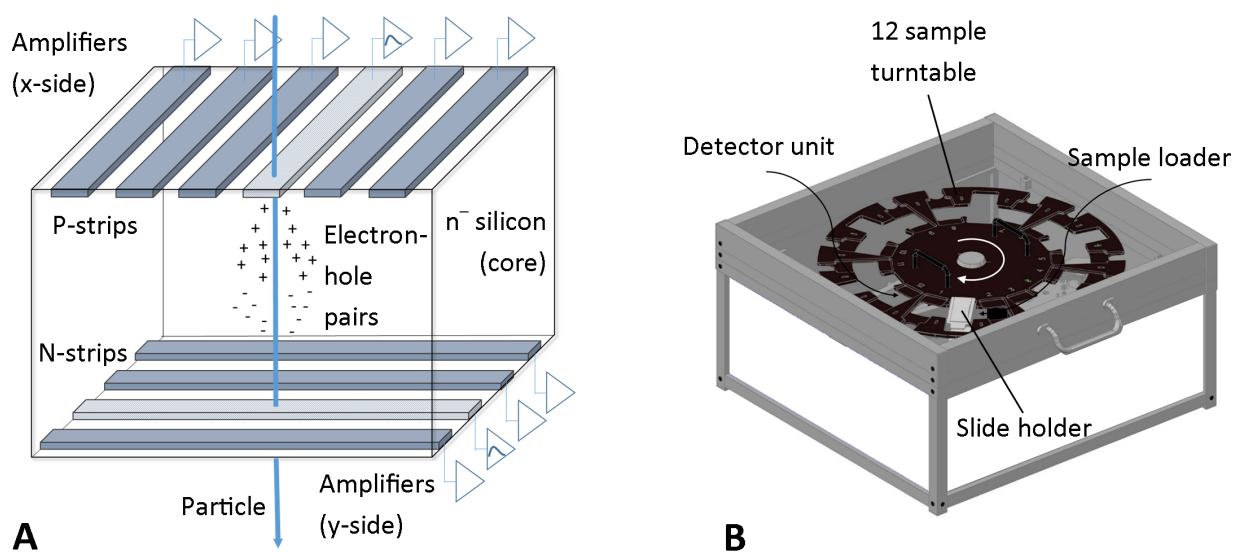
FIG. 1.

Schematics of the detection principle of the DSSD detector (A) and the entire digital autoradiography system, including the detector unit placed below a 12-sample sample-changing mechanism (B).

A small number of strips in any DSSD will either suffer from a failed connection to the read-out electronics resulting in no registered data, or malfunction, producing such a high level of background that these strips must be masked out to prevent contributing to the collected data. These are commonly referred to as dead or missing strips and the missing data will be interpolated from neighboring strips during image reconstruction. The number of disconnected or malfunctioning strips in our system were in total 57 corresponding to 3 % of all strips. However most of these were outside the field of view of the sample slide and include deliberately unconnected strips at the edges. Inside the relevant field of view a total of 13 strips were malfunctioning to some degree, corresponding to 0.7% of strips in that area.

2.B. Measurements of Detector Characteristics

Environmental background and noise

An empty microscope glass was placed in the slide holder, covered with Mylar foil and imaged in the detector for 52 hours with the dead or over-reporting strips masked so as not to contribute to the image. The image was reconstructed without any software corrections for missing or elevated strips and the total amount of counts determined.

Detection efficiency and energy spectra

In order to mirror the conditions of imaging a biological sample, homogenized chicken liver was used to create phantoms to determine the system detection efficiency. After ultra-sonic and mechanical homogenization of the liver sample a radionuclide solution was added. The different radionuclides used were $^{99m}TcO_4^-$, $^{111}InCl_3$, (Mallinckrodt Pharmaceuticals, Dublin, Ireland), ^{125}I-NaI, ^{131}I-NaI, (GE Healthcare, Buckinghamshire, UK), $^{177}LuCl$, $^{68}GaCl$ (IDB Holland, Holland) and ^{18}F, chosen because of their common use in preclinical research. $^{18}F^-$ was produced locally at Skåne University Hospital in Lund. The volume of each phantom was around 8 mL with an activity concentration of approximately 100 kBq per mL. To rid the

sample of air bubbles, the substance was centrifuged (1 min, 2000 rpm). Samples were frozen in embedding media (O.C.T., Tissue Tek, PA, USA) using dry ice and ethanol (>95%) and sectioned in 10 μm thick slices using a cryostat. For each radionuclide, 5 microscope slides with 3 sections were imaged for a minimum of 1 h each and the initial count rate at start of imaging determined from the data file. Adjacent sections were dissolved in HCl and measured in a well type gamma counter (Wallac WIZARD 1480, Wallac, Turku, Finland) to determine the activity per section. The measured energy spectrum for each radionuclide was also extracted from measurement data. No change was made to the factory energy calibration of the instrument. Efficiency was calculated by dividing the initial count rate with the corresponding decay-corrected activity.

System dead time

The effects of detector dead time were investigated for two different measurement geometries. A point source was simulated by placing a drop of approximately 5 kBq ^{18}F$^-$ activity on a piece of absorbing paper and a plane source covering the entire field of view by submerging absorbing paper in a ^{18}F solution from where it absorbed approximately 7 kBq. Count rates up to 4000 counts per second (cps) were measured and a non-paralyzable system response model[18] was used to determine the system dead time τ:

$$n = \frac{m}{1 - m\tau} \qquad (1)$$

Where *m* is the measured and *n* the expected count rate as determined by fitting the ^{18}F decay curve to data from count rates below 100 cps.

*Line source phantom from neutron activation of a nickel wire*

Because no thin enough line source was available commercially, a radioactive line source emitting suitable beta particles for spatial resolution measurements had to be produced. ^{58}Ni can be activated to ^{58}Co through a fast neutron induced reaction ^{58}Ni(n,p)^{58}Co. ^{58}Co has a half-life of 70.86 days and is a both a β^+-emitter (14.9% mean β^+-energy 201.1 keV) and γ-emitter (99.4% γ-energy 810.8 keV). The metastable state ^{58m}Co (half-life of 9.1 h, γ-energy 25 keV) is also formed in the same reaction, but after a few days only the ground state will remain. It should be noted that pure elemental nickel contains several isotopes, whose natural abundances are given in Table 1. Thus additional activities ^{65}Ni (half-life 2.52 h) and ^{57}Ni (half-life 35.60 h) are formed by the reactions ^{64}Ni(n,γ)^{65}Ni, and ^{58}Ni(n,2n)^{57}Ni, respectively. These are short lived compared to ^{58}Co, so after some weeks after neutron irradiation the remaining main activity is ^{58}Co.

TABLE 1. Isotopes of nickel in the wire that was neutron activated.

Nickel isotope	Natural abundance
^{58}Ni	68.077%
^{60}Ni	26.223%
^{61}Ni	1.14%
^{62}Ni	3.634%
^{64}Ni	0.926%

In order to activate nickel and to produce ^{58}Co, a thin nickel wire was irradiated at the 250 kW FiR 1 Triga Mark II research reactor, located in Espoo, Otaniemi, Finland. As the neutron

activation reaction ^{58}Ni(n,p)^{58}Co requires fast neutrons (5-15MeV) as indicated in Figure 2 showing the cross section for the reaction, the central thimble with a substantial fast neutron flux (thermal and fast neutron, fluxes are 1.0×10^{13} neutrons cm^{-2} s^{-1}) was chosen as the irradiation position.
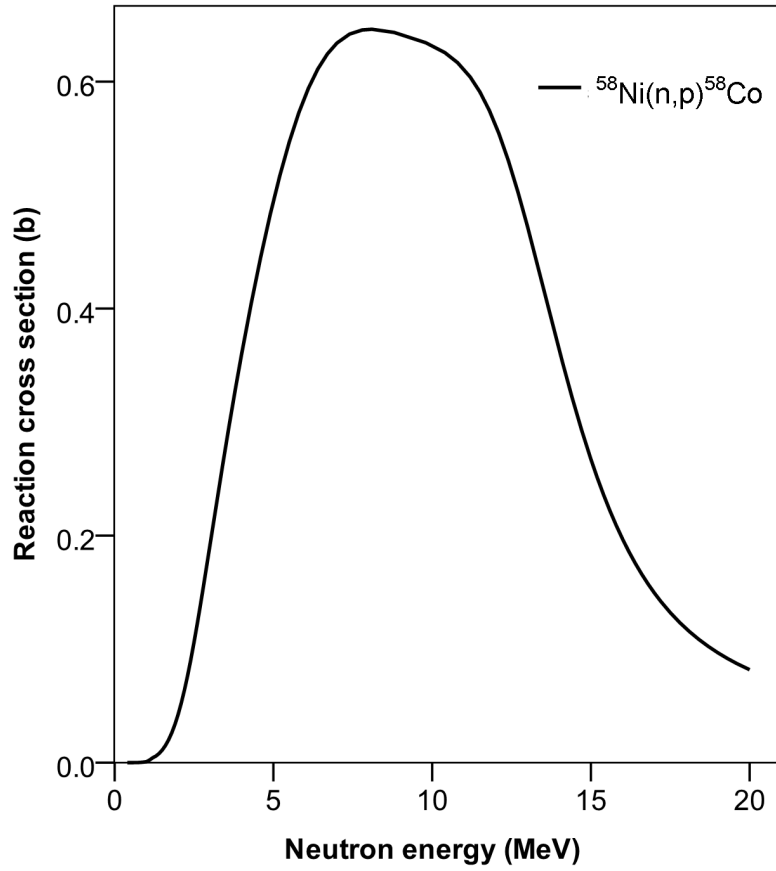
FIG. 2.

Cross section of the ^{58}Ni(n,p)^{58}Co reaction. Data from the International dosimetry and fusion file, IRDFF[19] (1 barn = 10^{-24} cm^2.). The necessary neutron energies in the interval 5-15 MeV were achieved in central parts of the reactor.

The wire used as per the supplier (Alfa Aesar, Karlsruhe, Germany) was 99.98% pure nickel and had a diameter of 10 μm. In order to irradiate the nickel wire in the reactor core, a 100 cm long wire (estimated mass 0.7 mg) spun on an anodized aluminum spool was put inside a standard watertight aluminum irradiation capsule, which was used for irradiations in the water filled central thimble of the FiR 1 reactor core. The total irradiation time of the nickel wire was 18 hours. The total measured [58]Co activity of the coil was 15 days after end of irradiation about 10 kBq, approximately 100 Bq/cm wire.

Due to embrittlement during irradiation, the wire had to be transferred from the spool by pressing pieces of pressure sensitive adhesive tape to the spool so that several lines of wire attached to it. When removed, the adhesive side of the tape formed an irregular array of line sources. One of these arrays was imaged using light microscopy to determine the condition of the wire and the thickness of the transferred wire was measured at twelve different sections.

The relative radionuclide composition in one of the transferred samples was determined by high resolution gamma spectroscopy using the APEX laboratory measurement software (Canberra, Meriden, Connecticut, USA). The sample was measured for 14 days, starting 38 days after end of bombardment (EOB). The detector used was an HPGe detector (Canberra SeGe, model GC5021, Canberra, Meriden, Connecticut, USA) placed behind a lead shield.

Spatial resolution

One of the line source arrays, placed on a sample slide, was selected and imaged for 93 hours using the DSSD system, 94 days after EOB, and subsequently for 144 hours, 105 days after EOB, inside a film cassette using a storage phosphor system (Cyclone Plus, Perkin Elmer, Wellesley, MA, USA). For both measurements the sample slide was placed in a sample holder and covered with 3 μm Mylar foil. The storage phosphor system had the read-out resolution set to its maximum 600 dots per inch, i.e. 42.3 micrometer per pixel. The image from the

DSSD system was reconstructed from list-mode data of all registered events without any software corrections using IDL 6.4 software (ITT Visual Information Solutions, Boulder, CO, USA). Both images were analyzed using ImageJ software[20], and an image area outside the radioactive sample was used to determine the background which was subtracted from both images. Five separate locations to acquire line profiles were then chosen per imagein order to reduce the influence of overlap. In these profiles, the maximum value was determined using a parabolic fit to the highest value point and its two closets neighbors. The full width at half maximum (FWHM) was then determined by measuring the distance between points calculated through linear interpolation between the points closest to half the maximum value of the profile, according to the NEMA NU-2012 method[21].

2.C. Application of multi-radionuclide imaging

A mouse preclinical animal study was performed as a proof-of-principle for employing the ability to separate contributions from several radionuclides also used for *in vivo* imaging or radionuclide therapy. All procedures involving animals were performed under approved protocols of the UCLA Animal Research Committee.

Intact chimeric monoclonal antibody (mAb) anti-CEA T84.66 (cT84.66)[22] and T84.66 diabody (scFv dimer of 55 kDa)[23] were radiolabeled with ^{125}I and ^{131}I, respectively, using the Iodo-Gen method as previously described[23]. Athymic nude (nu/nu) female mice (Charles River Laboratories, Wilmington, MA, USA), 7- to 8-week-old, were subcutaneously injected on the right shoulder region with $1\text{-}2 \times 10^6$ LS174T human colon carcinoma cells expressing carcinoembryonic antigen (CEA) (American Type Culture Collection, Manassas, VA).

Approximately 10 days after tumor inoculation, two LS174T tumor-bearing mice were injected intravenously (i.v.) with 12 MBq/101 μg of the ^{125}I-labelled intact cT84.66. At 67 h following the first injection the same mice were injected i.v. with 4 MBq/77 μg of the ^{131}I-

labelled T84.66 diabody. The mice were sacrificed at 6 h post-injection of the diabody which corresponded to 73 h, post-injection of the intact antibody. The tumor was excised, frozen and cryosectioned. Sections of 100 μm thickness were imaged using the DSSD system for 60-840 minutes. Thinner section of 30 μm thickness were stained with either Hematoxylin and Eosin or, using immunohistochemistry, for determination of the CEA antigen distribution and expression in the tumors. The separation of contributions from ^{125}I and ^{131}I was performed using IDL 6.4 software by best fit of previously acquired single-isotope spectra to binned energy data in each pixel as previously outlined in Örbom et al 2007[24]. For detector strips that had been identified as over or under reporting, their total amplitude was adjusted to a mean value of neighboring functional strips by either removing or duplicating randomly selected events in the data for that strip while maintaining the data in list-mode format. Similarly, faulty strips that contributed no signal where recreated in the image by randomly duplicating events from the closest functioning strips at a ratio corresponding to their distance to the faulty strip.

2.D. Application of energy discrimination

Characteristic x-rays at low energies are registered by the detector and contribute to degradation in spatial resolution due to their long path length compared to β or α particles. By applying an energy cut-off limit it is possible to exclude the contributions from these photons and to improve image quality. Minor image artifacts stemming from small differences in individual strip energy threshold are also mitigated by excluding lower energies. To evaluate this application on a biological sample, a section of a kidney from a mouse injected with an ^{111}In-labelled radiopharmaceutical prior to sacrifice was imaged using the DSSD system. Images were reconstructed with IDL 6.4 software, using all available events or only those with a measured energy of above or below 30 keV, thereby excluding the low energy

characteristic x-rays of [111]In. Image corrections for missing and miscalibrated strips were applied.

Images were evaluated in ImageJ. Regions, the same in all images, with low pixel value were compared to areas with higher pixel values and the ratio of mean pixel value $\bar{S}$ for different regions was used to estimate the contrast:

$$Contrast = \frac{\bar{S}_{high}}{\bar{S}_{low}} \qquad (2)$$

3. RESULTS

3.A. Background and noise

The signal measured on the detector with a non-radioactive sample is 1.18 counts per second for the whole field of view, which given 649687 non-masked pixel during imaging gives 1.81×10^{-6} counts per second per pixel. Using the Currie Equation[25], this leads to the minimum detectable count rate being 2.89×10^{-5} counts per second per pixel. The background events were evenly distributed over the image and the measured energy spectrum of the background (Figure 3) had a mean energy of 116 keV.
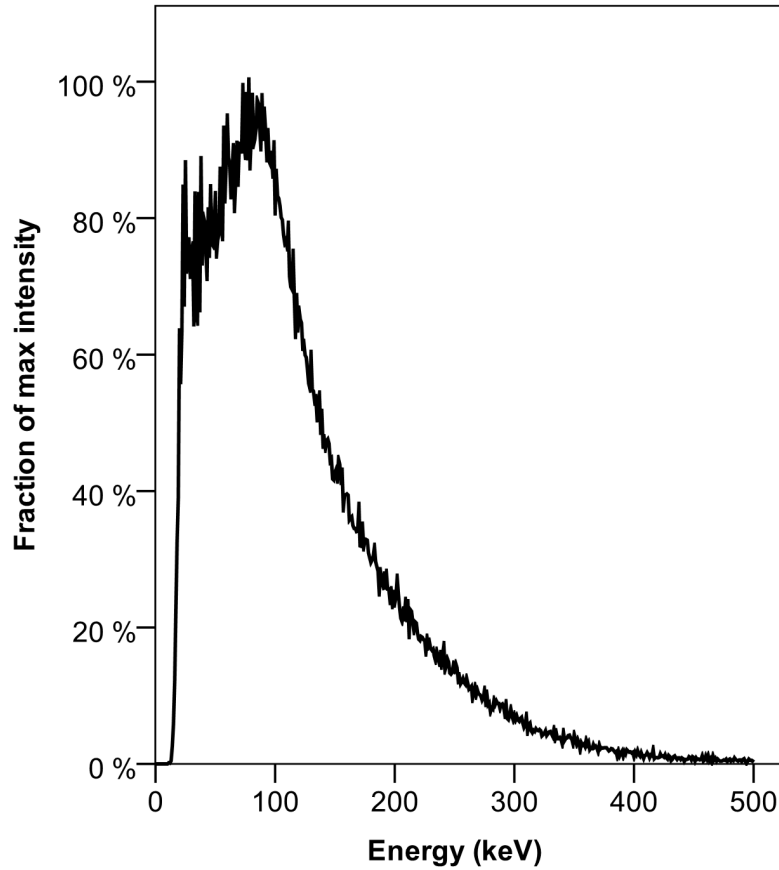
FIG. 3.

Energy spectrum of the background and noise as measured on the DSSD system. The measured background is 1.18 counts per second for the whole field of view and 1.81×10^{-6} counts per second per pixel.

3.B. Detection efficiency and energy spectra

The measured detection efficiency for each radionuclide is presented in Table 2. Energy spectra for three selected radionuclides (^{111}In, ^{99m}Tc and ^{18}F) can be found in Figure 4, as well as the β^+ emission spectrum of ^{18}F. The ^{18}F (max β^+ energy 633.5 keV) spectrum is similar to the measured energy distribution for higher energy β-emitter (data not shown) since their particle range will exceed the detector thickness and the resulting dE/dx spectra will be

similar, regardless of β energy. The spectrum for [superscript]111[/superscript]In on the other hand is dominated by an individual peak from low energy x-rays and Auger electrons at 19-23 keV with smaller peaks mainly from conversion electrons at 144 keV and 219-245 keV. Similarly, the measured ^{99m}Tc energy spectrum has a peak from conversion electrons at 120 keV and a smaller one from x-rays and Auger electrons at 15-21 keV. Whereas the peaks at the higher end of the ^{111}In and ^{99m}Tc spectra correspond well to their respective highest energy conversion electrons, the ^{18}F spectrum ends well before its max β energy of 633.5 keV. The point of maximum measured intensity of ^{18}F is also slightly lower than in the emission spectra due to lower detection efficiency at higher energies and energy loss before entering the detector. Relevant characteristics of each radionuclide for which efficiency was determined are listed in Table 3.

TABLE 2. Detection sensitivity for selected radionuclides on the DSSD autoradiography system.

Radionuclide	Sensitivity (cps/kBq) ±STD
^{99m}Tc	64±2
^{111}In	227±8
^{177}Lu	249±13
^{125}I	229±10
^{131}I	334±37

^{18}F	699±58
^{68}Ga	446±60
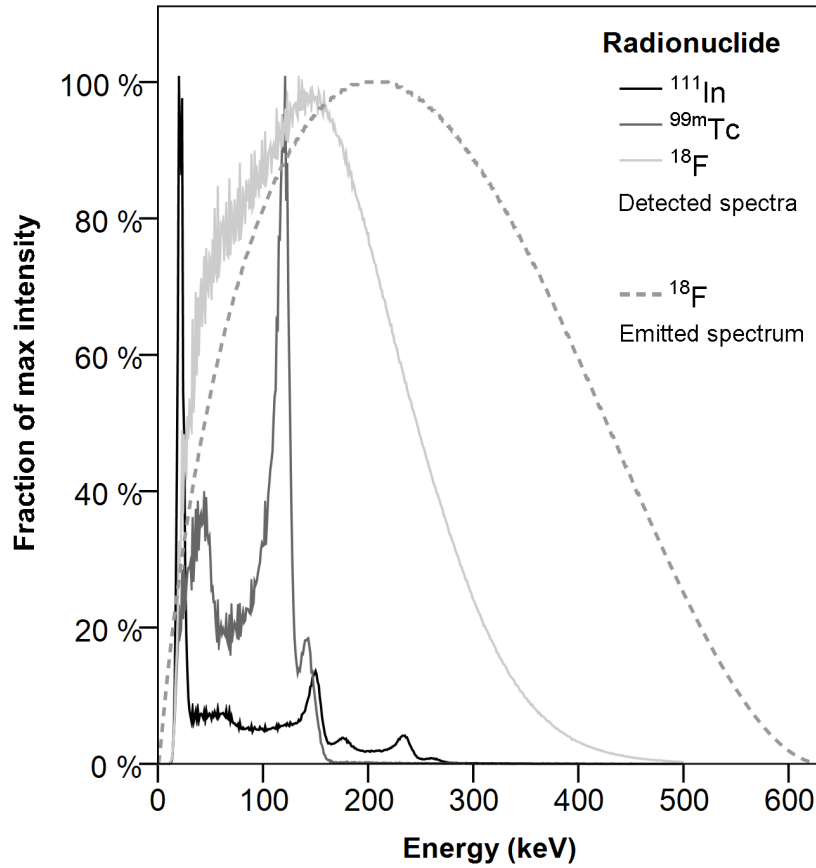
FIG. 4.

The individually normalized measured energy spectra of electrons and low energy photons of

^{18}F, ^{99m}Tc and ^{111}In as measured on the DSSD system. Also inserted, the ^{18}F β$^+$ emission

spectrum[26], for comparison.

TABLE 3. Relevant radiations of the radionuclides used for efficiency measurements. Data

retrieved from the National Nuclear Data Center web database in the MIRD format[27].

Radionuclide	Half-life	Type	Yield (%)	Avg. energy (keV)	Max energy (keV)
F-18	109.77 min	β+	96.7	249.8	633.5
In-111	67.32 hours	λ	90.6	171.3	
		λ	94.1	245.4	
		ce	7.87	144.6	
		X-ray	24.2	22,9	
		X-ray	45.4	23.2	
Lu-177	6.734 days	β-	79.4	149.6	498.3
		λ	10.4	208.4	
I-125	59.408 days	X-ray	73.5	27.47	
		X-ray	39.4	27.2	
		ce	10.7	30.55	
Tc-99m	6.001 hours	λ	89.0	140.5	
		ce	8.79	119.5	
I-131	8.02070 days	β-	89.6	191.6	606.31
Ga-68	67.629 min	β-	87.7	836.0	1899.1

3.C. System dead-time

Measurement data (Figure 5) was fitted numerically by the least-squares measure to the non-paralyzable dead time model (R^2=0,995), resulted in a system dead time constant τ at 59 µs. There was no observed dead time difference between the two measured geometries.
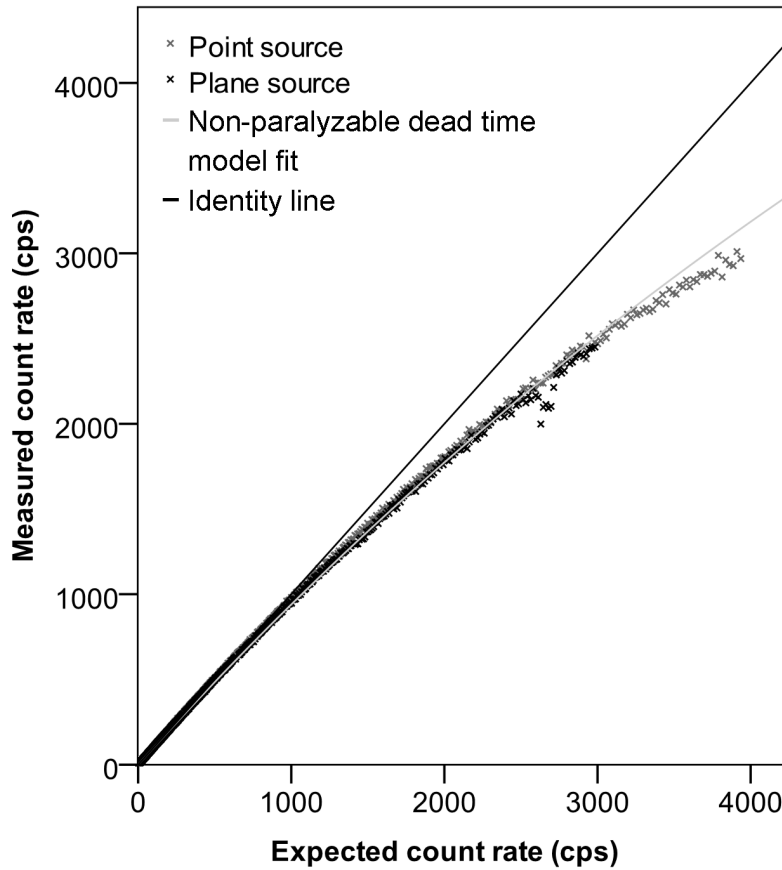
FIG. 5.

Measured count rates for two different geometries of ^{18}F plotted against expected count rates based on extrapolation from count rates below 100 cps. The solid line shows the non-paralyzable system response model fitted to the data with a calculated dead time constant of 59 us.

3.D. Line source phantom characteristics

Optical microscopy images of the irradiated wire revealed instances where the physical stress of transfer had bent or fragmented the wire but it was largely in similar condition as unirradiated wire. The mean wire diameter after irradiation and transfer was measured by optical microscopy to be 18.0 ±1.8 μm. The spectroscopy measurement showed almost all of the activity in the transferred wire sample to be ^{58}Co apart from the impurities ^{57}Co, ^{60}Co, ^{59}Fe, ^{57}Ni and ^{51}Cr. The impurities relative intensities were 0.1, 0.05, 0.005 percent for the cobalt and iron impurities and below quantifiable levels for ^{51}Cr and ^{57}Ni. When imaged in the DSSD system, a representative section of thread yielded 1.7 counts per second per cm 94 days after EOB.

Spatial resolution

Measurements on the images acquired from DSSD and storage phosphor systems (Figure 6) gave mean FWHM values of 154 ±14 μm for the DSSD system and 343 ±15 μm for the storage phosphor system.


3 mm
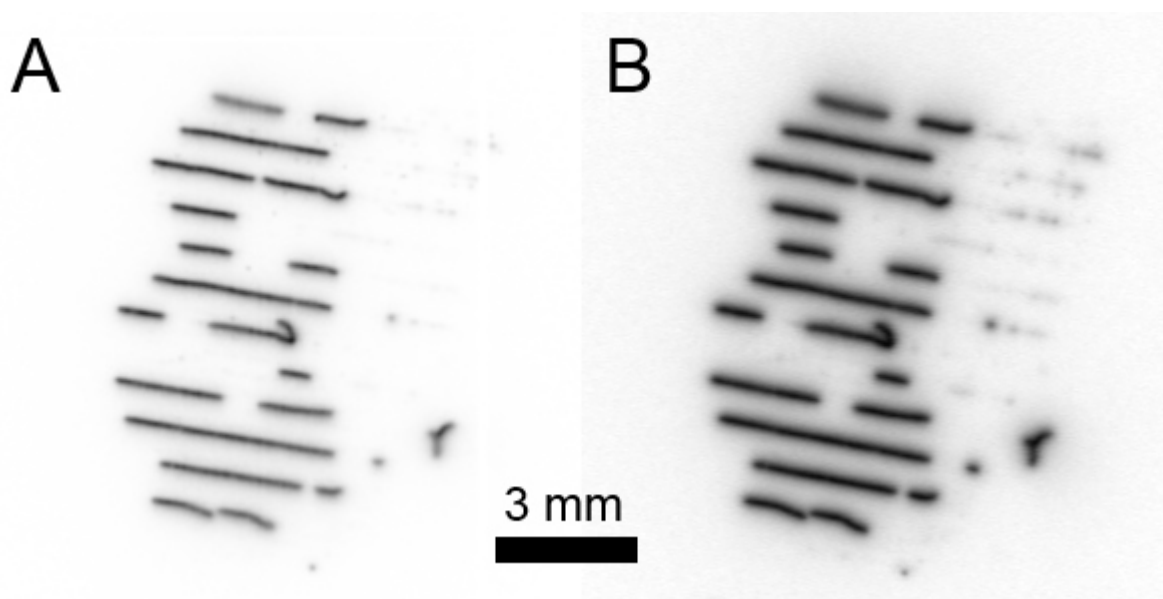
FIG. 6.

Digital autoradiography images of the same sample imaged in the DSSD system for 93 h (A) and in a storage phosphor screen system for 144 h and scanned at 600 dpi (B). The sample consists of ^{58}Co activity in sections of 18 μm thick ^{58}Ni wire after neutron irradiation in a research reactor and transfer from the original spool to a sample slide using adhesive tape due to embrittlement. Background has been subtracted from (B) and both images are individually scaled from zero (white) to maximum (black) intensity. FWHM was measured to 154 ±15 μm for the DSSD system and 344 ±14 μm for the storage phosphor system.

3.E. Intratumoral distribution of CEA radiotracers

Activity distributions of ^{125}I-cT84.66 mAb (Figure 7C) and the ^{131}I-diabody fragment (Figure 7A) were successfully reconstructed and visually compared to histology (Figure 7B) and antigen distribution (Figure 7D). As seen, both ^{125}I and ^{131}I activities are distributed throughout the tumor sections. Clear hotspots in areas with necrotic or interstitial tissue are seen with ^{125}I, whereas the ^{131}I activity is clearly elevated in areas of viable tumor cells with more pronounced CEA staining. The lower image quality of ^{125}I is also noticeable, stemming from the wider point-spread-function of the radionuclide due to the detector registering the low-energy x-rays further from the source of decay than is the case with β-particles.
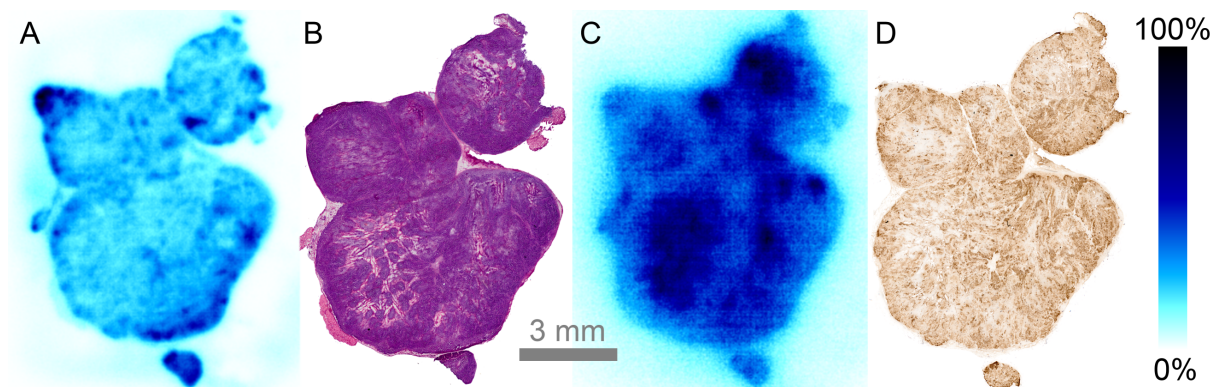
FIG. 7.

Adjacent tumor sections from one mouse administered ^{125}I-cT84.66 mAb and ^{131}I-T84.66 diabody that was sacrificed at 73 h post-injection of ^{125}I-cT84.66 mAb corresponding to 6 h post-injection of ^{131}I-T84.66 diabody. Digital autoradiography images are from a single imaging session of a single tumor section with the ^{131}I activity distribution (A) separated from the ^{125}I activity distribution (C) using energy data. Both individually scaled from no (white) to maximum (black) measured activity per pixel. Adjacent tumor sections, different from the one imaged by autoradiography, stained with hematoxylin and eosin (B) or, using immunohistochemistry, for CEA antigen (D).

3.F. Application of energy discrimination

Images of the ^{111}In sample were reconstructed from the same measurement data, using all events (Figure 8A) or only above (Figure 8B) or below (Figure 8C) 30 keV. The reduction in total number of image counts due to energy discrimination of counts below 30 keV was 44%. The discriminated image (Figure 8B) has visibly less spread of image signal outside the kidney section while having retained or improved level of detail inside the section. Mean contrast ratios between dark and light areas, measured in the same regions, for the original (Figure 8A) and discriminated image (Figure 8B) were found to be 1.8 and 2.2 respectively.

The contribution from events below 30 keV (Figure 8C) has visibly lower spatial resolution and poor contrast, suggesting that these events degrade image quality.
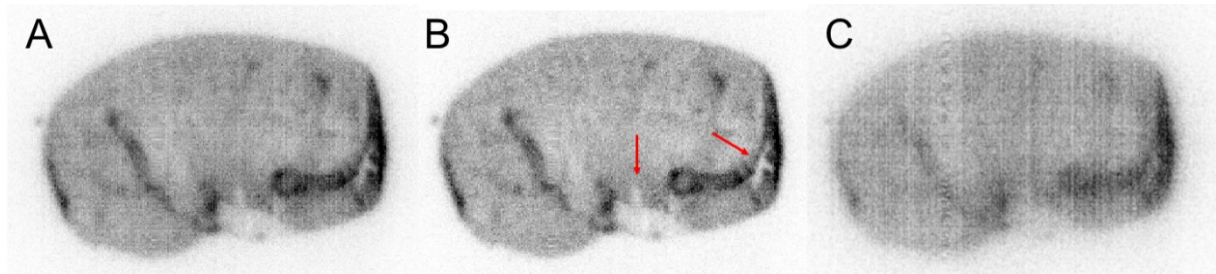
FIG. 8.

Uptake of an ^{111}In-labeled pharmaceutical in a kidney section. Using all events (A) or with energy discrimination discarding all signals below (B) or above (C) 30 keV. Note the decreased spread of detected events outside the section and the retained or increased (red arrows) level of discernible detail in (B) compared to (A), even though the total number of counts has been reduced by 44%. The grid-like artifacts stemming from small differences in strip response at low energies are also suppressed in B. All images use the same gray scale and are individually scaled from zero (white) to 70% of maximum (black) intensity.

4. DISCUSSION

Our characterization of the double-sided silicon strip detector (DSSD) digital autoradiography system shows that it could be gainfully employed as a complement to *in vivo* radionuclide imaging. As demonstrated in a small animal study, the system has the ability to separate the signal from several simultaneously imaged radionuclides using their energy spectra or rate of decay. The spatial resolution of ^{58}Co was measured to be better than on a commonly used storage phosphor screen system. The low background and noise allows for a comparatively

low minimum detectable count rate and measurements of the dead-time behavior of the detector show that while a correction factor will need to be applied when rates approach thousands of counts per second, high count rate samples can be quantitatively imaged.

In a preclinical *in vivo* imaging situation, the radionuclides used for labeling are often chosen on the grounds of having emissions detectable by PET or SPECT cameras, or for high efficacy radionuclide therapy. The range of isotopes employed in this study reflect those constraints. In other applications of autoradiography, ^{14}C and ^{3}H are the most commonly used radionuclides[1] with the latter not being detectable on the characterized DSSD system. A further limitation for application in high-throughput studies is the limited field of view of the DSSD, which does not allow for whole-body autoradiography of adult mice or larger animals, and not for simultaneous imaging of more than a few sections of excised organs. Using either longer-lived radionuclides or a high injected activity the latter issue can be somewhat alleviated by loading samples in the sample changer and imaging them sequentially. Small fields of view have been common for particle-counting digital autoradiography systems, although recently a 168 cm^2 field of view CMOS detector has been developed[11]. In applications where the tracer biodistribution is determined by *in vivo* imaging and digital autoradiography is used for more specific and qualitative purposes, such as imaging the intratumoral distribution of a new tracers, a small field of view will be less of an issue.

While the detector characteristics measured in this study can be taken as a general guideline to system performance, each DSSD system will have individual levels of noise and inactive or overactive strips that will require different energy thresholds as well as detector masking. The seemingly much lower spatial resolution of the storage phosphor system may partly be an effect of the ^{58}Co isotope emitting x-rays that have energies below the DSSD system detection limit but that will be registered by the storage phosphor screen. This could reverse for an isotope like ^{125}I where the thicker detection layer of the DSSD system will register the low

energy x-rays from ^{125}I with a much longer path length, while they are less likely to interact in the thinner storage phosphor screen.

In a table comparing modern digital autoradiography systems, Esposito et al[12] reports measured spatial resolution FWHM values for ^{14}C ranging from 20 μm for a system based on contact imaging through a solid scintillator sheet[5] to 79.5 μm for a CMOS based system[28]. These values, as well as the reported ^{14}C sensitivities are not directly comparable to our measurements due to different measurement methodology and because ^{14}C has a lower mean beta energy of 49 keV compared to 201 keV for [58]Co and therefore is expected to have a smaller FWHM. Using Monte Carlo simulations in 2010, Cabello and Wells show that for a silicon detector, there is limited benefit of pixel sizes below 10 μm for ^{14}C imaging due to electron range[2], so for higher-energy beta emitters, 50 μm pixels may not dramatically degrade spatial resolution. Two systems catalogued by in Esposito et al[12] report smallest detectable count rate per area and these are approximately one order of magnitude smaller than for the DSSD system in this work.

Other commercially available autoradiography systems with the ability to separate radionuclides based on emission spectra are to our knowledge two systems marketed by Biospace Lab (Paris, France) based on contact imaging through a solid scintillator sheet or a parallel plate avalanche chamber respectively, both employing an image intensifier tube and CCD camera[5]. The DSSD system studied here have comparable spatial resolution to the latter (150 μm FWHM for ^{18}F) but not the former (20 μm for ^{14}C), which does however have a smaller detection area (24 mm x 32 mm)[5]. Direct detection of charged particles as in the DSSD system should give a better energy resolution and therefore better ability to separate radionuclides than indirect measurement via scintillation light.

Neutron activation of a thin ^{58}Ni wire was employed to produce a ^{58}Co line source used to determine the spatial resolution. However the extensive embrittlement caused during irradiation made the wire very difficult to handle and any similar future attempts should consider pre-mounting the wire in an imaging geometry on top of a material not sensitive to neutron activation before irradiation.

The small animal study described here provides an example of an application where multi-radionuclide imaging could be successfully employed to compare the intratumoral distribution of two radiolabeled tracers in the same animal. The distribution of ^{125}I-labeled intact antibody to more necrotic areas that show less staining of CEA is in line with previously published studies on the distribution of iodine-labeled anti-CEA antibodies in tumor xenograft models[29,30]. This may be the result of an initial lack of penetration of the larger antibody molecules (150 kDa) into the more dense areas of viable tumor cells[31,32] or a result of the radionuclide being released from the antibody or the antibody itself including pooling of the radiolabel in the blood subsequent to the initial uptake[30]. The distribution of the ^{131}I activity indicates that the smaller diabody fragment preferentially distributes to viable tumor cells although a larger study, including additional time points would be required to investigate this question. Another labeling scheme, such as DPTA-^{111}In/^{177}Lu, not sensitive to dehalogenation or autoradiography image degradation from x-rays should be employed in such a future study, possibly along with *in vivo* imaging using multi-radionuclide SPECT/CT.

5. CONCLUSIONS

This study has shown that a DSSD system can be beneficially applied for digital autoradiography with simultaneous multi-radionuclide imaging capability, complementing *in vivo* radionuclide imaging. System benefits include a low background signal, ability to image both low and high activity samples, and a good energy resolution, while the main drawback is

a small field of view. Proof of concept was shown in a preclinical radioimmunodiagnostic setting, simultaneously imaging ^{125}I and ^{131}I.

6. AKNOWLEDGEMENTS

R EFERENCES

[1]   E.G. Solon, "Use of Radioactive Compounds and Autoradiography to Determine Drug Tissue Distribution," Chem Res Toxicol **25**, 543-555 (2012).

[2]   J. Cabello, K. Wells, "The spatial resolution of silicon-based electron detectors in beta-autoradiography," Phys Med Biol **55**, 1677-1699 (2010).

[3]   P. Johnstrom, J.L. Bird, A.P. Davenport, "Quantitative phosphor imaging autoradiography of radioligands for positron emission tomography," Methods Mol Biol **897**, 205-220 (2012).

4   R.F. Johnston, S.C. Pickett, D.L. Barker, "Autoradiography using storage phosphor technology," Electrophoresis **11**, 355-360 (1990).

5   N. Barthe, K. Chatti, P. Coulon, S. Maitrejean, B. Basse-Cathalinat, "Recent technologic developments on high-resolution beta imaging systems for quantitative autoradiography and double labeling applications," Nucl Instrum Meth A **527**, 41-45 (2004).

6   L.Y. Chen, L.S. Gobar, N.G. Knowles, D.W. Wilson, H.H. Barrett, "Direct Charged-Particle Imaging System Using an Ultra-Thin Phosphor: Physical Characterization and Dynamic Applications," IEEE Trans. Nucl. Sci **56**, 2628-2635 (2009).

7   T. Back, L. Jacobsson, "The alpha-camera: a quantitative digital autoradiography technique using a charge-coupled device for ex vivo high-resolution bioimaging of alpha-particles," J Nucl Med **51**, 1616-1623 (2010).

8   K. Ljunggren, S.E. Strand, "Beta camera for static and dynamic imaging of charged-particle emitting radionuclides in biologic samples," J Nucl Med **31**, 2058-2063 (1990).

9   J.E. Lees, G.W. Fraser, P. Carthew, "Microchannel plate detectors for C-14 autoradiography," IEEE Trans. Nucl. Sci **45**, 1288-1292 (1998).

10   J. Cabello, A. Bailey, I. Kitchen, M. Prydderch, A. Clark, R. Turchetta, K. Wells, "Digital autoradiography using room temperature CCD and CMOS imaging technology," Phys Med Biol **52**, 4993-5011 (2007).

11   M. Esposito, T. Anaxagoras, J. Larner, N.M. Allinson, K. Wells, "C-14
        autoradiography with a novel wafer scale CMOS Active Pixel Sensor," J Instrum **8,**
        (2013).

12   M. Esposito, G. Mettivier, P. Russo, "C-14 autoradiography with an energy-sensitive
        silicon pixel detector," Phys Med Biol **56**, 1947-1965 (2011).

13   M. Overdick, A. Czermak, P. Fischer, V. Herzog, A. Kjensmo, T. Kugelmeier, K.
        Ljunggren, E. Nygard, C. Pietrzik, T. Schwan, S.E. Strand, J. Straver, P. Weilhammer,
        N. Wermes, K. Yoshioka, "A "Bioscope" system using double-sided silicon strip
        detectors and self-triggering read-out chips," Nucl Instrum Meth A **392**, 173-177
        (1997).

14   B. Sanghera, R. Ott, "Preliminary studies using silicon strip detectors in digital
        autoradiography," IEEE Trans. Nucl. Sci **40**, 992-995 (1993).

15   A. Orbom, S.E. Eriksson, E. Elgstrom, T. Ohlsson, R. Nilsson, J. Tennvall, S.E.
        Strand, "The intratumoral distribution of radiolabeled 177Lu-BR96 monoclonal
        antibodies changes in relation to tumor histology over time in a syngeneic rat colon
        carcinoma model," J Nucl Med **54**, 1404-1410 (2013).

16   S. Evans-Axelsson, D. Ulmert, A. Orbom, P. Peterson, O. Nilsson, J. Wennerberg, J.
        Strand, K. Wingardh, T. Olsson, Z. Hagman, V. Tolmachev, A. Bjartell, H. Lilja, S.E.
        Strand, "Targeting free prostate-specific antigen for in vivo imaging of prostate cancer
        using a monoclonal antibody specific for unique epitopes accessible on free prostate-
        specific antigen alone," Cancer Biother Radiopharm **27**, 243-251 (2012).

17   R. Madru, P. Kjellman, F. Olsson, K. Wingardh, C. Ingvar, F. Stahlberg, J. Olsrud, J. Latt, S. Fredriksson, L. Knutsson, S.E. Strand, "99mTc-labeled superparamagnetic iron oxide nanoparticles for multimodality SPECT/MRI of sentinel lymph nodes," J Nucl Med **53**, 459-463 (2012).

18   G.F. Knoll, *Radiation detection and measurement*, 3rd ed. (John Wiley & Sons, New York, 2000).

19   E.M. Zsolnay, R. Capote, H.K. Nolthenius, A. Trkov, "Summary description of the new international dosimetry and fusion file (IRDFF release 1.0), Technical report INDC(NDS)-0616," (IAEA, Vienna, 2012).

20   Rasband, W.S., "ImageJ," U. S. National Institutes of Health, Bethesda, Maryland, USA, http://imagej.nih.gov/ij/, (1997-2014).

21   N.E.M. Association, *NEMA standards publication NU 2-2012: performance measurements of positron emission tomographs*. (National Electrical Manufacturers Association, Rosslyn, USA, 2013).

22   M. Neumaier, L. Shively, F.S. Chen, F.J. Gaida, C. Ilgen, R.J. Paxton, J.E. Shively, A.D. Riggs, "Cloning of the Genes for T84.66, an Antibody That Has a High Specificity and Affinity for Carcinoembryonic Antigen, and Expression of Chimeric Human Mouse T84.66 Genes in Myeloma and Chinese Hamster Ovary Cells," Cancer Res **50**, 2128-2134 (1990).

23   A.M. Wu, L.E. Williams, L. Zieran, A. Padma, M. Sherman, G.G. Bebb, T. Odom-Maryon, J.Y.C. Wong, J.E. Shively, A.A. Raubitschek, "Anti-carcinoembryonic

antigen (CEA) diabody for rapid tumor targeting and imaging," Tumor Target **4**, 47-58 (1999).

[24] A. Orbom, M. Dahlbom, T. Olafsen, A.M. Wu, S.E. Strand, "Serial digital autoradiography with a silicon strip detector as a high resolution imaging modality for TRT Dosimetry," IEEE Nucl Sci Conf R 2007, Vols 1-11, 4054-4056 (2007).

[25] G.F. Knoll, *Radiation detection and measurement*, 3rd ed. (Wiley, New York, 2000).

[26] S. Chu, L. Ekström, R. Firestone, "WWW Table of Radioactive Isotopes, database version 2/28/1999," http://nucleardata.nuclear.lu.se/nucleardata/toi, (2014).

[27] Brookhaven National Laboratory, "Nuclear Decay Data in the MIRD Format," http://www.nndc.bnl.gov/mird/, (2014).

[28] J. Cabello, A. Bailey, I. Kitchen, R. Turchetta, K. Wells, "A dual threshold method to independently control spatial resolution and sensitivity in β imaging," IEEE Nucl Sci Conf R 2008, 1-7 (2008).

[29] A.A. Flynn, G.M. Boxer, R.H.J. Begent, R.B. Pedley, "Relationship between tumour morphology, antigen and antibody distribution measured by fusion of digital phosphor and photographic images," Cancer Immunol Immun **50**, 77-81 (2001).

[30] J.L.J. Dearling, A.A. Flynn, U. Qureshi, S. Whiting, G.M. Boxer, A. Green, R.H.J. Begent, R.B. Pedley, "Localization of radiolabeled anti-CEA antibody in subcutaneous and intrahepatic colorectal xenografts: influence of tumor size and location within host organ on antibody uptake," Nucl Med Biol **36**, 883-894 (2009).

[31] S.H. Jang, M.G. Wientjes, D. Lu, J.L.S. Au, "Drug delivery and transport to solid tumors," Pharm Res-Dordr **20**, 1337-1350 (2003).

[32] I.K. Choi, R. Strauss, M. Richter, C.O. Yun, A. Lieber, "Strategies to increase drug penetration in solid tumors," Front Oncol **3**, 193 (2013).